Dendritic GABAergic inhibition controlled by Shh signaling-dependent stellate cell pool is critical for motor learning

Wen Li[1#], Lei Chen[1#], Jonathan T. Fleming[1], Emily Brignola[1], Kirill Zavalin[2], Andre H. Lagrange[2], Tonia S. Rex[3], Shane A. Heiney[4], Gregory J. Wojaczynski[5], Javier F. Medina[5] and Chin Chiang[1*]

[1]Department of Cell and Developmental Biology, Vanderbilt University School of Medicine, 4114 MRB III, Nashville, TN 37232

[2]Department of Neurology, Vanderbilt University Medical Center, 6135 MRB III, Nashville, TN 37232

[3]Department of Opthalmology & Visual Science, Vanderbilt Eye Institute, 11435 MRBIV, Nashville, TN 37232

[4]Iowa Neuroscience Institute, University of Iowa, Iowa City, IA 52242

[5]Department of Neuroscience, Baylor College of Medicine, S709 Houston, TX 77030

Running title: Molecular layer interneuron subtype

Keywords: Cerebellum, neurogenesis, Sonic hedgehog, interneuron subtypes, dendritic synapses and motor learning.

#These authors contributed equally
*Address all correspondence to: Chin Chiang

chin.chiang@vanderbilt.edu

Tel: (615) 343-4922

SUMMARY

Cerebellar inhibitory interneurons are important regulators of neural circuit activity for diverse motor and non-motor functions. The molecular layer interneurons (MLI), consisting of basket cells (BCs) and stellate cells (SCs), are generated sequentially from Pax2+ immature interneurons which migrate from the prospective white matter to the ML of the cortex. However, little is known as to how MLI subtype identities and pool sizes are determined, nor are their contributions to motor learning well-understood. Here, we show that GABAergic progenitors fated to generate BCs and SCs transiently respond to the Shh signal. Conditional abrogation of Shh signaling reduced the number of $Pax2^{+}$ cells, whereas persistent Shh pathway activation increased their numbers. These changes did not affect BC numbers but selectively altered the SC pool size. Moreover, genetic depletion of GABAergic progenitors when BCs are generated resulted in a specific reduction of SCs, suggesting that the specification of MLI subtypes is independent of their birth order and occurs after $Pax2^{+}$ cells settle into their final laminar positions. Mutant mice with reduced SC numbers displayed decreased dendritic inhibitory synapses and neurotransmission onto Purkinje cells, resulting in an impaired acquisition of eyeblink conditioning. These findings reveal an essential role of Shh signaling-dependent SCs in regulating inhibitory dendritic synapses and motor learning.

INTRODUCTION

The cerebellum plays an essential role in fine motor learning characterized by an adaptive process that involves recurring error-evoked learning to maintain optimum motor performance (Raymond and Medina, 2018). The circuit that enables this mode of learning is comprised of different classes of inhibitory and excitatory neurons that are generated during embryonic and postnatal development from spatially distinct progenitors (Hoshino et al., 2005; Machold and Fishell, 2005;

Palay and Chan-Palay, 1974a; Wang et al., 2005; Zhang and Goldman, 1996). However, it remains unclear how their identities and numbers are specified to generate a functional circuit.

Purkinje cells (PCs) are the sole projection neurons in the cerebellar cortex, with a dendritic plane in the molecular layer where they integrate excitatory and inhibitory input from different sources (Beckinghausen and Sillitoe, 2018). The principal excitatory neurons are granule cells with their axons extending into the molecular layer as parallel fibers that provide excitatory input to PCs. Additionally, PCs receive excitatory input from two classes of extracerebellar afferent projections; climbing fibers of the inferior olive nuclei terminate in the molecular layer and contact PCs, and mossy fibers (from the brainstem and elsewhere) synapse with granule cells and thus influence many PCs at once. The balance to the excitatory neurotransmission is provided largely by GABAergic inhibitory inputs from molecular layer interneurons (MLIs) that consist of basket cells (BCs) and stellate cells (SCs) (Sotelo, 2015). BCs are located in the inner one-third of the ML, and their axons form perineuronal nests or "baskets" as well as specialized structures known as pinceau around the PC soma/axon initial segment (Somogyu and Hámori, 1976). In contrast, SCs occupy the rest of the ML and make direct contact with distal PC dendrites. Despite the apparent morphological and positional differences between BCs and SCs, the precise location and the boundary between these two cell types have not been well defined until the recent identification of Ret, a receptor tyrosine kinase, whose expression is restricted to BCs (Sergaki et al., 2017).

Cerebellar inhibitory neurons are generated from spatially distinct germinal zones. In mice, the early-born neurons, including PCs, Golgi (granule layer interneuron), and Lugaro cells, are generated from the ventricular zone (VZ) of the fourth ventricle during early to mid-embryonic stages (Hoshino et al., 2005; Sudarov et al., 2011). The late-born MLIs are generated sequentially but in an overlapping manner from the prospective white matter (PWM) during the late embryonic

to postnatal development, with BCs emerging first and followed by SCs (Zhang and Goldman, 1996). Recent studies have identified stem cell-like astroglia in the PWM as the source of transient amplifying GABAergic progenitors marked by Ptf1a (Fleming et al., 2013), a bHLH transcription factor whose function is required for the specification of all GABAergic lineages, including $Pax2^{+}$ immature interneuron (Hoshino et al., 2005; Pascual et al., 2007). $Pax2^{+}$ cells migrate from PWM to ML before terminally differentiating into BCs and SCs (Weisheit et al., 2006). However, it remains unclear as to how MLI subtype identities are determined.

The Shh signaling pathway has been shown to play critical roles during cerebellar development. It is required for the rapid expansion of granule cells by promoting the proliferation of granule cell precursors (Dahmane and Altaba, 1999; Wallace, 1999; Wechsler-Reya and Scott, 1999). Additionally, Shh signaling is transiently required to maintain the proliferative capacity of multipotent radial glial cells in the VZ and astroglia in the PWM (Fleming et al., 2013; Huang et al., 2009). Unlike VZ, Ptf1a+ progenitors are proliferative and exhibit Shh pathway activity in the PWM (Fleming et al., 2013). However, the significance of this activity in the regulation of MLI pool size and cerebellar function has not been determined. While recent studies have shown that MLIs play an important role in cerebellar-dependent motor learning (Brinke et al., 2015; Sergaki et al., 2017), it remains to be determined as to what extent each MLI subtype contributes to motor learning. In this study, we investigated the role of Shh signaling and its contribution to MLI subtype allocations and cerebellar-dependent motor learning.

RESULTS

Shh signaling is transiently activated in Ptf1a+ progenitors in the PWM

To better define Shh signaling in GABAergic progenitors, we used β-galactosidase (β-gal) expression from Gli^{nlacZ} mice (Bai et al., 2002) to assess Shh pathway responsiveness among $Ptf1a^{+}$

cells at different postnatal stages. We found that Shh signaling is transiently activated in a subset of Ptf1a+ cells from P1 to P8 (Figure 1A), while contemporaneous populations of Ptf1a^{+} cells in the brain/ brainstem were negative for the signal. At P1, the β-Gal+ and Ptf1a+ cells account for ~19% of Ptf1a+ progenitors in the PWM, and this number increased to ~26% at P3 (Figure 1B and 1C). However, at P6, the percentage of double-positive cells declined to ~14%, but no statistically significant changes were observed for Ptf1a+ progenitors (Figure 1B and 1C). By P8, a very small population of Ptf1a+ progenitors were positive for β-gal expression (Figure 1C). Thus, the Shh pathway is transiently activated in a subset of Ptf1a^{+} progenitors.

To ascertain the significance of Shh signaling in Ptf1a^{+} progenitors, we blocked Shh reception by genetically ablating the transducer Smo using the GABAergic lineage-specific *Ptf1a^{cre}* line (Kawaguchi et al., 2002). Our initial analysis of the mature cerebellar cortex of *Ptf1a^{Cre}; Smo$^{F/-}$* mutant mice at P30 detected no structural or layering alterations; thickness of the molecular layer, granule layer, overall cerebellar area, and foliation pattern was comparable to the control (Figure 1D-1F). However, there is a clear reduction of hematoxylin/eosin-stained cells in the molecular layer. Indeed, immunohistochemical (IHC) detection of the calcium-binding protein, parvalbumin, which preferentially marks MLIs and PCs, showed a statistically significant decrease in the total number of MLIs in *Ptf1a^{Cre}; Smo$^{F/-}$* mutant cerebella (Figure 1D and 1G). The most reduction was most prominent in the outer half of the ML, suggesting that a germinal program was biased towards the stellate interneuron subtype (see below). The number of other early-born inhibitory neurons, including PCs and Golgi cells expressing Calbindin and Neurogranin, respectively, was not significantly changed in *Ptf1a^{Cre}; Smo$^{F/-}$* mutants (Figure 1H and 1I).

Shh signaling regulates precursor pool expansion through Ccnd2

To understand how Shh signaling affects the MLI pool size, we evaluated the proliferation and survival of Ptf1a progenitors in the PWM. Following a short-term (1h) labeling with the thymidine analog EdU, we observed a significant reduction of proliferating Ptf1a progenitors in *Ptf1a^{Cre}; Smo$^{F/-}$* mutants at both P3 (~20%) and P6 (~34%) when compared to controls (Figure 2A-2C). Accordingly, the total number of Ptf1a+ progenitors in the mutant was reduced by ~30% and ~68% at P3 and P6, respectively (Figure 2B and 2C). Viability was measured with cleaved-Caspase-3, but no appreciable changes were found in Ptf1a lineage cells at either P3 or P6 (Figure S1).

Genetic fate-mapping studies have shown that Ptf1a^{+} cells emerge upstream of and contribute considerably to neonatal Pax2^{+} immature interneuron pools (Fleming et al., 2013). The peak of Pax2 production in PWM occurs at P5, where they subsequently migrate to ML through the inner granule layer (IGL) before terminally differentiating into BCs and SCs (Weisheit et al., 2006). We measured the abundance of Pax2^{+} cells at P6 and observed a significant reduction of their numbers in PWM, IGL, and ML (Figure 2D-H).

The role of Shh signaling in promoting Ptf1a progenitor proliferation was further evaluated using a gain-of-function approach. We generated *Ptf1a^{cre}; SmoM2* mice by crossing the *Ptf1a^{Cre}* driver strain to *SmoM2* conditional mutants that harbor a constitutively activated form of *Smo* (Mao et al., 2006). Consistent with the loss of function study, we observed a significant increase in the number of Ptf1a+ progenitors (~27%) as well as their proliferative capacity (~15%) in *Ptf1a^{cre}; SmoM2* cerebella when compared to controls at P6 (Figure 2I-2K). Accordingly, the number of Pax2+ cells is also significantly increased (Figure 2L and 2M). Together, we provide strong evidence for a direct and essential role of Shh signaling in driving the proliferation of Ptf1a+ progenitors in PWM and subsequent expansion of Pax2+ immature interneurons.

To determine how Shh signaling promotes Ptf1a progenitor proliferation, we performed RNA-seq analysis and compared the transcriptomes of *Ptf1a*^{Cre}*; Smo*$^{F/-}$ mutant and control cerebella at P3 using PWM and adjacent tissues, that are mainly devoid of EGL and GL, collected from laser capture microdissection (Figure 2S). The differential expression score was then determined using the generalized fold-change (GFOLD) algorithm (Feng et al., 2012) in which differentially expressed genes were ranked by including both raw fold change and variance of the posterior distribution of log fold change. A total of 440 (GFOLD ≤-0.5) genes were downregulated including *Smo, Ptf1a,* and *Pax2* (Table S1). The lack of *Gli1* in this list is likely attributed to its relatively strong expression level in the Bergmann glia when compared to progenitors in the PWM (Fleming et al., 2013). The gene ontology analysis identified 22 genes that are associated with positive regulation of cell proliferation (Fig. 2N). In particular, *Cyclin d2* (*Ccnd2*) is expressed in the PWM and required for the proliferation of MLI progenitors (Huard et al., 1999), but the signal that activates its expression is unknown. We confirm that the number of Ccnd2+ GABAergic progenitors is significantly reduced in the *Ptf1a*^{Cre}*; Smo*$^{F/-}$ PWM by immunohistochemistry (Figures. 2O and 2P). These data suggest that Shh signaling regulates Ptf1a progenitor cell proliferation through activation of Ccnd2.

Specification of MLI subtypes occurs independent of their birth orders

To determine whether specific MLI subtypes are affected in *Ptf1a*^{Cre}*; Smo*$^{F/-}$ mutants, we acquired the *Ret*^{GFP} mouse line in which EGFP reporter is expressed from the endogenous Ret promoter (Jain et al., 2006). Consistent with previous studies (Sergaki et al., 2017), *Ret*^{GFP} expression in BCs is first detectable at P7 and continues throughout adulthood (Figure S3A). Outside of the ML, *Ret*^{GFP} is expressed in the deep cerebellar nuclei (DCN) and associated fibers in PWM (Figure S3B and S3C),

but not in Pax2+ interneuron progenitors as reported previously (Sergaki et al., 2017). The Ret+ DCN neurons are NeuN positive but GABA negative, indicating that they are not GABAergic neurons (Figure S3D). Therefore, *Ret*^{GFP} expression is confined to mature BCs and DCN neurons. In addition to *Ret*^{GFP} expression, we incorporated Parvalbumin (Parv) as a marker to highlight all MLIs. In this way, BCs and SCs can be unambiguously identified as Ret^{GFP+} Parv^{+} and Ret^{GFP-} Parv^{+} cells, respectively. Using these markers, we were able to determine that SC numbers were reduced by ~21% in *Ptf1a*^{Cre}*; Smo*$^{F/-}$ mutant cerebella (Figure 3A and 3B) whereas no appreciable changes in BC numbers were observed when compared to that of controls (Figure 3A and 3C).

Classical birthdating and genetically inducible fate mapping (GIFM) studies have suggested that MLI subtype identities are correlated with their birth dates and laminar positions within the cerebellar cortex (Leto et al., 2006; Sudarov et al., 2011). To determine if the subtype-specific effect of Shh signaling on MLIs is associated with temporal differences in Shh responsiveness of Ptf1a^{+} progenitors fated to generate both BCs and SCs, we generated *Ptf1a*^{creER}*; Ai9; Ret*^{GFP} line to perform GIFM study focusing on critical stages where Shh signaling is activated in Ptf1a progenitors. Tamoxifen (TM) administration at P0 marked both BCs (dtTomato^{+} Ret^{GFP+}) and SCs (dtTomato^{+} Ret^{GFP-}) in the molecular layer at P21, representing ~21% and ~79% of all marked cells, respectively (Figure 3D, 3E and 3F). Moreover, marked BCs account for ~56% of all Ret^{GFP+} cells (Figure 3G), indicating that the peak of BC production occurs between P0 and P1. When TM was administered at P3, marked BCs decreased to ~30% (Figure 3G), with a concomitant increase in marked SCs (Figure 3F). At P5, SCs are the only labeled population present in the ML (Figure 3F and 3G). Therefore, BCs and SCs are both generated at the time when Shh signaling is active in Ptf1a+ progenitors, and the differential effect of Shh signaling on MLI subtypes is unlikely due to temporal difference in Shh responsiveness. Indeed, analysis of *Ptf1a*^{cre}*; SmoM2* mutants with constitutive Shh

pathway activation in Ptf1a^{+} progenitors showed that only Ret^{GFP-} Parv^{+} (SC) numbers are elevated whereas the Ret^{GFP+} Parv^{+} (BC) pool remained unchanged when compared to the control (Figure 3H-K).

The observation that altered numbers of Pax2^{+} immature interneuron in the Shh signaling mutants had no effect on BC pool size suggests that the commitment to the BC fate does not occur until they settle into the inner ML. Accordingly, the BC pool remains unchanged as long as there are sufficient Pax2^{+} cells to fill the inner ML. To further test this model, we generated *Ptf1a^{cre}; Ret^{GFP}*; *ROSA26^{DTR}* mice designed to temporarily ablate Ptf1a^{+} progenitors and their descendent Pax2^{+} cells. The *ROSA26^{DTR}* line expresses the Cre-inducible Diptheria toxin receptor (DTR) that triggers cell ablation upon exposure to Diptheria toxin (DT). Administration of DT at P0-P2, a time when Ptf1a^{+} progenitors are fated to generate most BCs, resulted in a drastic reduction of Pax2^{+} immature interneurons in all layers of the cerebellum at P6 (Figure 3L-3P). Despite ~50% reduction of total Pax2^{+} cells (Figure 3M), we observed no effect on BC numbers while SCs are reduced by ~49% (Figure 3Q – 3T). Collectively, the results suggest that MLI subtypes are specified independent of their birth order but likely occur at their laminar positions, providing a mechanism by which Shh signaling is selectively promoting the expansion of SCs.

Impaired GABAergic synapses and inhibitory control over PCs

In the mature cerebellum, SCs and BCs relay inhibitory input to PCs via direct synapses on dendritic tree or somata/proximal initial segment, respectively, balancing excitatory input received from granule neurons and afferent fibers (Sotelo, 2015). To understand how the loss of Shh-dependent SCs might impact the integrity of cerebellar neural circuitry, we evaluated the distribution of specific molecular markers for inhibitory and excitatory synapses in the ML. We used a presynaptic marker,

vesicular GABAergic transporters (VGAT), in combination with a postsynaptic marker Gephyrin to highlight inhibitory synapses. In the ML, the number of inhibitory synapses (puncta with co-localization) at PC dendrites was reduced by 31% in *Ptf1a*^{Cre}*; Smo*$^{F/-}$ mutants compared to controls (Figures 4A-4C). We also used another inhibitory presynaptic marker, glutamic acid decarboxylase 67 (Gad67), which is responsible for up to 90% of GABA synthesis in the brain (Asada et al., 1996; Kash et al., 1997), and found that its puncta are also significantly reduced (Figure S4). Consistent with unperturbed BC development, the number of inhibitory synapses at PC soma and the pinceau marked by the potassium voltage-gated channel 1.2 (Kv1.2) remains similar between *Ptf1a*^{Cre}*; Smo*$^{F/-}$ mutants and controls (Figures 4D and 4E). However, VGluT1 (Figures 4F and 4H), which labels excitatory synaptic terminals at granule cell parallel fibers, showed no significant changes, nor did VGluT2 (Figures 4G and 4I), which marks excitatory synaptic terminals at climbing fibers. Altogether these findings show substantial impairment to the inhibitory component of the cerebellar system in *Ptf1a*^{Cre}*; Smo*$^{F/-}$ mutants, while the excitatory component appears to be unperturbed.

The significantly reduced number of dendritic inhibitory synapses in *Ptf1a*^{Cre}*; Smo*$^{F/-}$ mice suggests impaired neurotransmission. To directly test this, we performed whole-cell patch-clamp recordings on cerebellar slices to compare spontaneous inhibitory postsynaptic currents (sIPSCs) of PCs as a measure of inhibitory synaptic strength in wild-type (n=10) and mutant (n=8) mice. This analysis revealed that adult *Ptf1a*^{Cre}*; Smo*$^{F/-}$ mice had about a 35% decrease in the frequency of sIPSCs when compared to the control (Figure 5A-5C). Similarly, the amplitude of sIPSCs is also significant reduced in *Ptf1a*^{Cre}*; Smo*$^{F/-}$ mice (Figure 5B). These findings indicate that PCs lose dendritic synapses and show attenuated inhibitory input.

Diminished capacity for associative motor learning

To determine whether the reduction of dendritic inhibitory neurotransmission on PCs might impair cerebellum-dependent functions, a series of neurobehavioral assays were performed. The cerebellum is classically known to coordinate motor function, and the most obvious manifestation of cerebellar impairment is abnormal gait. *Ptf1a*^{Cre}*; Smo*$^{F/-}$ mice did not demonstrate gross impairments in mobility, such as ataxia, nor were they observed to show clinical signs of tremor. When subjected to treadscan analysis, adult *Ptf1a*^{Cre}*; Smo*$^{F/-}$ (n=12) and control mice (n=11) showed comparable gait, which is divided into three basic components: i) stance (break + propulsion), ii) swing, and iii) stride (stance + swing), and is measured in both length and time (Figures 6A-6E). To test motor learning, these animals were also subjected to an accelerating rotarod assay. On the first day of testing sessions, mutant and control animals showed nearly identical latency to fall, indicating that no obvious differences in motor coordination, balance, or strength were detectable (Figure 6F). However, during the subsequent days, it appeared that *Ptf1a*^{Cre}*; Smo*$^{F/-}$ mutants had an apparent deficiency in the ability to learn to perform this task, with statistically significant shorter latencies to fall than controls (Figure 6F). Overall, loss of a SC subset did not appear to adversely impact gross motor function in *Ptf1a*^{Cre}*; Smo*$^{F/-}$ mutants and only imparted a subtle impairment to primitive motor learning.

Proper cerebellar function is also necessary for delay eyeblink conditioning, a form of associative motor learning required for multi-sensory integration that is often impaired in autistic individuals (Medina et al., 2000; Sears et al., 1994). The paradigm involves pairing a neutral conditioned stimulus (CS; e.g., LED light pulse or tone) with an eyeblink-evoking unconditioned stimulus (US; e.g., an air puff). After repeated CS-US pairing, an association is progressively established such that the eyelid conditioned response (CR), in the form of learned blink, occurs before the onset of the US. We, therefore, determined whether cerebellum-dependent eyeblink

conditioning is compromised in *Ptf1a*^{Cre}*; Smo*$^{F/-}$ mice with reduced SC numbers. In this paradigm, a blue LED light pulse was used as the CS for a period of 240 ms followed immediately by a gentle air puff for 40 ms (Figure 6G). Eyelid movement was measured using a high-speed infrared camera interfaced with MATLAB (Heiney et al., 2014) and the eyelid position was assigned to a value between 0 (fully open) and 1 (fully closed). After 14 days of consecutive sessions of conditioning (1400 trials in total), *Ptf1a*^{Cre}*; Smo*$^{F/-}$ mice had a consistently lower amplitude of eyelid closure just before CS exposure when compared to control mice (Figure 6H and 5S). Although both the mutant and control mice showed a gradual increase in the percentage of CRs, mutant mice had significantly lower CRs throughout the conditioning sessions (Figure 6I).

While the Shh pathway has not been reported to be active in the retina of Ptf1a-expressing cells and their lineage, we were concerned that the CR deficit in *Ptf1a*^{Cre}*; Smo*$^{F/-}$ mutants is due to compromised retina function. We, therefore, performed electroretinograms (ERG) and visual evoked potentials (VEP) to assess retinal and visual pathway activity in response to light. We observed no significant differences in maximum responses of rod photoreceptors (a_{max}), inner retinal neurons (b_{max} and oscillatory potentials; OP), or the visual cortex (VEP N1) between *Ptf1a*^{Cre}*; Smo*$^{F/-}$ and control mice (Figure S6), indicative of normal retinal and visual pathway function. To confirm that the mutants have a deficit in associative motor learning, we also used a tone as CS in delayed eyeblink conditioning. Similar to LED light, the mutant mice showed a diminished response to the tone as presented by the lower amplitude of eyelid closure and percentage of CRs (Figure 6J, 6K, S5). Collectively, these results indicate that Shh signaling-dependent dendritic synapses formation plays a critical role in associative motor learning.

DISCUSSION

MLIs constitute the majority of inhibitory interneurons in the cerebellum, but the mechanisms that regulate their subtype identities and pool sizes remain not well understood. Through genetic loss and gain of function studies, we demonstrate that the Shh signaling pathway acting through Ccnd2 in GABAergic progenitors is selectively required for the expansion of SCs. We reveal that the identities of MLI subtypes appear to be specified at their laminar positions independent of their birth order. Our studies at the synaptic and behavioral levels show that dendritic GABAergic inhibition controlled by Shh signaling-dependent SC pools is critical for motor learning.

Previous studies have shown that MLIs originate from multipotent astroglia in the PWM (Fleming et al., 2013; Parmigiani et al., 2015; Silbereis et al., 2009). These astroglia act as resident stem-like cells and proliferate in response to the Shh signal from PCs to generate astrocyte precursors as well as Ptf1a progenitors (Fleming et al., 2013). Our finding that Shh signaling is directly required for the proliferation of Ptf1a+ progenitors and subsequent expansion of MLIs offers an additional mechanism by which Shh regulates MLI pool size.

It is estimated that approximately 90% of all inhibitory neurons in the cerebellum are represented by late-born GABAergic interneurons (Weisheit et al., 2006). These neurons come from Pax2-expressing immature interneurons that are mostly generated during the first week of postnatal life (Weisheit et al., 2006). As $Pax2^{+}$ cells descend from $Ptf1a^{+}$ progenitors (Fleming et al., 2013) and emerge at the final progenitor cell division, Shh-induced proliferation of Ptf1a+ progenitors, therefore, serves as the main driver for their rapid expansion. This mode of regulation is in contrast to other regions of the nervous system where Shh pathway activity is generally excluded from postmitotic Ptf1a expressing cells. In the spinal cord, Ptf1a expression is restricted to the postmitotic progenitors in the dorsal neural tube whereas the Shh pathway is activated in the ventral domain (Bai et al., 2004; Glasgow et al., 2005). Moreover, ectopic Ptf1a expression is

correlated with the downregulation of the Shh signaling pathway as observed in Danforth's short tail mice (Orchard et al., 2018). Similarly, in the developing retina, Shh signaling is activated in early retinal progenitors whereas Ptf1a expression is restricted to postmitotic horizontal and amacrine cells (Fujitani et al., 2006). Indeed, the lack of Shh pathway activity in postmitotic retinal lineage cells is consistent with the absence of visual impairment in *Ptf1a*$^{cre/+}$*; Smo*$^{F/-}$ mice (Figure S5). Therefore, the Shh signaling pathway appears to be co-opted for the rapid expansion of Ptf1a^{+} progenitors to ensure an adequate supply of MLIs. Mechanistically, Ccnd2 is an attractive target that mediates the proliferative effect of Shh pathway activation on MLI progenitors. Unlike Ccnd1, Ccnd2 is strongly expressed in MLI progenitors and loss of Ccnd2 impairs their production (Huard et al., 1999). Reduced expression of Ccnd2 in Smo-deficient Ptf1a progenitors is consistent with the Shh pathway regulating Ccnd2 expression.

It has been reported that cerebellar MLIs undergo limited programmed cell death during the first two weeks of postnatal development (Yamanaka et al., 2004). More recent studies showed that GDNF signaling is required for the survival of MLIs. Genetic deletion of GDNF receptor GFRa1 or Ret in GABAergic progenitors resulted in a ~25% reduction of MLIs (Sergaki et al., 2017). Interestingly, the loss of NeuroD2, a bHLH transcription factor required for MLI differentiation, also promotes MLI survival (Pieper et al., 2019). Thus, MLI pool size is regulated at multiple levels by distinct mechanisms, from the proliferation of multipotent astroglia and Ptf1a progenitors to the survival of MLIs.

Fate mapping and heterochronic transplantation studies have suggested that MLI identities and laminar placement link to birthdate within the cerebellar cortex (Altman and Bayer, 1997; Cameron et al., 2009; Leto et al., 2009; Sudarov et al., 2011). Accordingly, a reduction in Ptf1a+ progenitors and Pax2+ immature interneurons as observed in *Ptf1a*$^{cre/+}$*; Smo*$^{F/-}$ mutants would have

a profound effect on the production of both BCs and SCs. It is, therefore, unexpected to discover that *Ptf1a*$^{cre/+}$*; Smo*$^{F/-}$ mutants did not affect BC production. This is not due to a lack of Shh responsiveness of Ptf1a+ progenitors fated to generate BCs as our *Ptf1a*^{CreER} GIFM study showed that BCs are largely generated from P0 to P3 when the majority of Shh responsive Ptf1a+ progenitors are present. Additionally, *Gli1*^{CreER} GIFM studies have shown that both MLI subtypes are generated from Shh-responsive progenitors (Fleming et al., 2013). The fact that the increased Pax2+ cell number observed in *Ptf1a*$^{cre/+}$*;SmoM2* mutants did not affect BC pool size further suggests that the commitment to BC and SC fates is not directly related to their birth order but appears to occur at laminar positions in an inside out sequence. Accordingly, Pax2^{+} cells that initially populate the inner ML acquire BC identity whereas those remaining in the outer ML assume SC fate. This model is further supported by our genetic ablation experiment in which the reduction of Ptf1a+ progenitors at the peak of BC production did not affect BC numbers despite a drastically diminished number of Pax2^{+} cells. Thus, changes in Pax2^{+} pool sizes as observed in Smo gain and loss-of-function mutants will have the greatest impact on SC numbers. Our model is consistent with the plastic nature of cerebellar immature interneurons observed from heterochronic transplantation studies (Leto et al., 2009), and it also explains why the preferential reduction of SCs in the ML is observed in *Ccnd2* and *Ascl1* mutants despite an early loss of interneuron progenitors (Huard et al., 1999; Sudarov et al., 2011).

Recent studies have shown that immature GCs play an instructive role in differentiation of SCs at the ML (Cadilhac et al., 2021). At present, Ret is the only marker that is selectively expressed in the BCs. Thus, understanding how its expression is activated may provide insight into how laminar positional information affects BC's identity. Ret has been studied extensively in the context of kidney and enteric nervous system development (Costantini, 2016; Lake and

Heuckeroth, 2013). Its expression in the ureteric bud and enteric neural crest-derived precursor cells is activated by retinoic acid (RA) signaling (Mendelsohn et al., 1999; Simkin et al., 2013). However, analysis of RA signaling using RA responsive reporter mice indicated that it is only activated in a subset of PCs, not in the BCs (Figure S7). Another possibility is that BCs identity is specified through an activity-dependent mechanism as proposed for the cortical interneuron specification (Wamsley and Fishell, 2017). There is evidence that the patterning of BC pinceau is shaped by PC activity (Zhou et al., 2020). In this context, Ret expression may be activated when the pinceau is established between its axon collaterals and the PC axon initial segment (AIS). Future studies are required to determine how positional information influences BC identity.

Previous studies have shown that the reduction of MLIs or the loss of their postsynaptic receptors γ2 GABA-A resulted in an impaired motor learning (Brinke et al., 2015; Sergaki et al., 2017; Wulff et al., 2009). However, it is unclear to what extent each MLI subtype contributes to motor learning. There are critical anatomical and functional differences in how SCs and BCs provide feed-forward inhibition of PCs in response to PF and CF activation. SCs primarily transmit chemical inhibition through axo-dendritic synapses whereas BCs deliver both chemical and electrical field inhibition through axo-somatic and axo-axonic synapses, respectively (Blot and Barbour, 2014; Korn and Axelrad, 1980; Palay and Chan-Palay, 1974b). Recent tamoxifen-mediated temporal deletions of the GABAergic transporter have suggested that BCs and SCs may have a distinct function in regulating PC simple spike firing pattern and rate (Brown et al., 2019). Our analysis of Shh signaling mutants provides evidence that SCs contribute significantly to motor learning. We found that the 21% reduction of SC numbers had a profound consequence on the cerebellar circuitry, resulting in a nearly 31% reduction in dendritic inhibitory synapses and significant impairment of inhibitory neurotransmission. This impairment in dendritic synapses

and GABAergic input onto PCs is sufficient to cause motor learning deficit. It remains to be determined whether axo-somatic and axo-axonic synapses contribute to motor learning.

ACKNOWLEDGEMENTS

We thank Jingqiong Kang, Ph.D. and Chun-Qing Zhang, M.D. for their initial help with electrophysiology experiments. We thank Christopher Wright, D.Phil. for the generous gift of antibody against Ptf1a. This study was supported by grants to C.C. from the Vanderbilt-Ingram Cancer Center Support Grant P30 CA068485 and the National Institutes of Health NS 097898.

AUTHOR CONTRIBUTIONS

C.C. designed the experiments and wrote the paper with the help of W.L. and L.C. W.L. performed all the experiments except eyeblink conditioning and ERG. W. L. performed the electrophysiology experiment with the help of K.A.Z. and A.H.L. L.C., W.L. and J.T.F. performed eyeblink conditioning experiment with the help of S.A.H., G.J.W. and J.F.M. The ERG data was provided by T.S.R. C.C., W.L. and L.C. analyzed data.

DECLARATION OF INTERESTS

The authors declare no competing interests.

KEY RESOURCES TABLE

Reagent or Resource	Source	Identifiers	Additional information
Antibody			
Rabbit monoclonal anti - β-Gal	ICL lab Cat#RGAL-45A-Z	Cat#RGAL-45A-Z RRID: AB_2885032	1:4000

Goat polyclonal anti-Ptf1a	(Fleming et al., 2013)	NA	1:8000
Mouse monoclonal anti - Parvalbumin	EnCor Biotechnology	Cat# MCA-3C9, RRID: AB_2572372	1:1000
Rabbit monoclonal anti - Calbindin	Cell Signaling Technology	Cat# 2173, RRID:AB_2183553	1:500
Chicken monoclonal anti - GFP	Aves Labs	Cat# GFP-1020, RRID:AB_10000240	1:1000
Rabbit monoclonal anti - Pax2	Thermo Fisher Scientific	Cat# 71-6000, RRID:AB_2533990	1:500
Mouse monoclonal anti - NeuN	Millipore	Cat# MAB377, RRID:AB_2298772	1:500
Cyclin D2	Santa Cruz Biotechnology	Cat# Sc452 RRID: AB_627350	1:100
Guinea pig polyclonal anti - VGAT	Synaptic Systems	Cat# 131 004, RRID:AB_887873	1:500
Mouse monoclonal anti - Gephyrin	Synaptic Systems	Cat# 147 011, RRID:AB_887717	1:500
Mouse monoclonal anti - vGluT1	Millipore	Cat# MAB5502, RRID:AB_262185	1:1000
Rabbit polyclonal anti - vGluT2	Synaptic Systems	Cat# 135 403, RRID:AB_887883	1:100
Mouse monoclonal anti - Kv1.2	Millipore	Cat# MABN77, RRID:AB_10806493	1:1000
Rabbit monoclonal anti - Cleaved Caspase-3	Cell Signaling Technology	Cat# 9661, RRID:AB_2341188	1:500
Mouse monoclonal anti - Gad67	Synaptic Systems	Cat# 198 211, RRID:AB_2721099	1:100
Goat anti - mouse Alexa Fluor 488	Thermo Fisher Scientific	Cat# A-11017, RRID:AB_2534084	1:500
Goat anti - rabbit Alexa Fluor 488	Thermo Fisher Scientific	Cat# A-11008, RRID:AB_143165	1:500
Goat anti - mouse Alexa Fluor 568	Thermo Fisher Scientific	Cat# A-11004, RRID:AB_2534072	1:500
Goat anti - rabbit Alexa Fluor 647	Thermo Fisher Scientific	Cat# A-21244, RRID:AB_2535812	1:500

Goat anti - chicken Alexa Fluor 488	Thermo Fisher Scientific	Cat# A-11039, RRID:AB_2534096	1:500
Donkey anti - goat Alexa Fluor 647	Thermo Fisher Scientific	Cat# A-21447, RRID:AB_2535864	1:500
Donkey anti - rabbit Alexa Fluor 488	Thermo Fisher Scientific	Cat# A-21206, RRID:AB_2535792	1:500
Reagent	**Source**		**Identifier**
Chemicals, Peptides, and Recombinant Proteins			
DAPI	Sigma		D9542
EdU	Click Chemistry Tools		1149-500
Tamoxifen	Millipore		156738
Corn oil	Sigma		C8267
KAPA2G Fast HotStart Genotyping Mix	Millipore		2GFHSGKB
Nacl	Sigma		S7653
Kcl	Sigma		P9333
$Mgcl_2 \cdot 6H_20$	Research Products International		7791-18-6
KH_2PO_4	Sigma		P0662
$NaHCO_3$	Sigma		S5761
$Cacl_2 \cdot 2\ H_2O$	Sigma		223506
D-glucose	Sigma		G8270
Cscl	Sigma		289329
HEPES	Sigma		H3375
EGTA	Research Products International		67-42-5
Mg-ATP	R&D System		B-20
GTP	Sigma		GE27-2076-01
CNQX	Millipore		3266820
APV	Sigma		A5282
Diphtheria toxin			
Animal models	**Source and Identifier**		
$Gli1^{nlaz}$	The Jackson Laboratory. Stock No.008211. (Bai et al., 2002)		
$Ptf1a^{Cre/+}$	(Kawaguchi et al., 2002)		
$Smo^{F/F}$	The Jackson Laboratory. Stock No.008211. (Long et al., 2001)		
SmoM2	The Jackson Laboratory. Stock No.005130. (Jeong et al., 2004)		
$Ret^{GFP/+}$	The Jackson Laboratory. Stock No. 029846. (Jain et al., 2006)		
$Ptf1a^{CreER/+}$	The Jackson Laboratory. Stock No.019378. (Kopinke et al., 2012)		

Ai9	The Jackson Laboratory. Stock No.007905. (Madisen et al., 2010)
iDTR	The Jackson Laboratory. Stock No.007900. (Buch et al., 2005)

EXPERIMENTAL PROCEDURES

Mice

All procedures followed animal care and biosafety protocols approved by Vanderbilt University Division of Animal Care in accordance with NIH guidelines. Histological analyses were carried out at postnatal (P) 1 to P30. Behavior experiments used 3 to 5 months adult mice. The following mouse lines were used in this study:

1. *Gli1*^{nlaz}, nlacZ reporter was inserted into the endogenous *Gli1* locus, creating a null allele and activating nlacZ expression in a pattern indistinguishable from that of *Gli1* (Bai et al., 2002). 2. *Ptf1a*$^{Cre/+}$, Cre was inserted into the endogenous Ptf1a locus, creating a null allele and activating Cre expression in a pattern indistinguishable from that of *Ptf1a* (Kawaguchi et al., 2002). 3. *Smo*$^{F/F}$, the loxP sequence was inserted on either side of exon 1 at the Smo locus, permitting a Cre recombinase dependent *Smo* loss of function mice (Long et al., 2001). 4. *R26*^{SmoM2}, *a lox-stop-lox eYFP SmoM2* cassette was inserted into *ROSA26* locus, permitting the expression of eYFPSmoM2 fusion protein in a Cre dependent manner (Jeong et al., 2004). 4. *Ret* $^{GFP/+}$, exon 1 of the *Ret* locus was replaced by eGFP, creating a null allele and activating eGFP expression in a pattern similar to that of *Ret* (Jain et al., 2006). 5. *R26*^{iDTR}, a loxp cassette containing diphtheria toxin receptor (DTR) was inserted into *ROSA26* locus, permitting the expression of DTR in a Cre dependent manner (Buch et al., 2005). 6. *R26R*^{Ai9}, a *CAG lox-stop-lox tdtomato* cassette was inserted into *ROSA26* locus, permitting the expression of tdtomato under the control of CAG promoter in a Cre-dependent manner (Madisen et al., 2010).

Mice treatments

For proliferation analysis, P3 and P6 pups were injected intraperitoneally with 50 mg/kg of EdU (5-ethyl-2-deoxyuridine; Sigma). Brains were harvested 2h after injection and processed for frozen tissue sections. Fate mapping studies, P0, P3 and P5 pups were injected intraperitoneally with 50 mg/kg of tamoxifen (Sigma) dissolved in corn oil. Brains were harvested at P21 and processed for frozen tissue sections as described below. P0 Pups were injected intraperitoneally with 3ng of Diptheria toxin daily for three consecutive days for cell ablation experiments. Brains were harvested at P6 or P21 for frozen tissue sections.

Tissue processing for histological analysis

Brains were retrieved from P0 to P8 after cervical dislocation and from deeply anesthetized adults after transcardial perfusion with 4% paraformaldehyde (PFA). Animals were anesthetized with 100mg/kg ketamine and 5 mg/kg of Xylazine. Brains were then fixed with 4% PFA for 48 hours at 4°C and processed for paraffin embedding. Sections of 5 mm were then collected on glass slides (Fisher) and paraffin was removed using xylene in a 3-wash series (1 x 10 minutes, 2 x 5 minutes). Sections were rehydrated with a descending EtOH series (100% (2x), 95%, 75%, 50%) 3 minutes each followed by two 1-minute washes in H_2O. Sections were stained with hematoxylin and eosin solution.

Immunohistochemistry

Immunohistochemistry analyses were performed on frozen tissue sections. Fixed brain tissues described above were rinsed with PBS and immersed in 30% sucrose solution before embedding in tissue freezing medium (OCT). Frozen tissues were sectioned on the Leica CM1950 cryostat at

15 mm. Endogenous peroxidases were blocked with 3% H_2O_2 in MeOH (5 mL 30% H_2O_2 in 45 mL 100% MeOH for 10 minutes followed with a 1x PBS wash for 3 x 5 minutes. Sections were incubated with PBS blocking solution containing 10% normal goat or donkey serum and 0.1% Triton X-100 at room temperature for 1 hour. A moisture chamber was prepared and slides placed into it. 100 µL of primary antibody (prepared in PBS blocking solution) per slide was added and each was covered with a coverslip and allowed to sit overnight at 4°C. The following day, coverslips were removed and slides were washed in 1x PBS, 3 x 5 minutes each. 100 µL of secondary antibody per slide was added and each was covered with a coverslip and allowed to sit for 1 hour at room temperature. Slides were washed in 1x PBS, 3 x 5 minutes each and were mounted using Fluorosave (Millipore) before imaging. For EdU detection, sections were incubated in PBS with 0.1M CuSO4, 0.1M THPTA, 2mM Azide 488, 1M L- Ascorbic at room temperature for 30min. Sections were washed 3x5minutes in PBS and then incubated with 5 µg/ml DAPI at room temperature for 10 minutes. All fluorescent images were acquired on Leica DMi8 microscope or Zeiss LSM 700 confocal microscope, processed using Leica LAS X or Zeiss Zen software and analyzed using NIH ImageJ.

Laser-capture microdissection (LCM) for the isolation of prospective white matter (PWM) for RNA-sequencing

P3 cerebella were retrieved, washed in cold PBS, and embedded in OCT compound. A series of 20µm sections were cut across the sagittal plane using Leica CM1950 cryostat and collected onto PEN membrane slides (Arcturus, ThermoFisher). The integral PWM was retrieved using a laser capture microdissection (LCM) system (ArcturusXT, ThermoFisher) according to manufactural instruction. Samples were collected in RNA lysis buffer, and RNA were extracted using RNeasy

Micro kit (Qiagen, 74004).

Rotarod test

Motor coordination and learning were tested using a commercially available (Harvard Apparaus) accelerating rotarod. The cylinder was 3 cm in diameter and was covered with textured rubber. Mice were confined to a section of the cylinder 5.7 cm wide by grey plastic dividers. The height to fall was 16 cm. Mice were placed on the accelerating rotarod whose speed gradually increased from 4 to 40 rpm over the course of a 300s trial. The time taken for the mouse to fall from the rotating rod was recorded. Mice that fell in less than 15 s were given a second trial. Occasionally, mice clung to the rod, and the whole animal rotated along with it. This behavior was classified as a "rotation," and the time at which this occurred for the first time on each trial was also recorded for each mouse. Thus the rotarod score was defined as latency to fall or to the first rotation, whichever occurred first. Three sessions were conducted on consecutive days, with three trials per session.

Gait analysis

Mice were placed on a translucent treadmill at a standstill. The treadmill was then turned on at a speed of 20 cm/s, and still images of their paw movements and placements were taken with a high-speed video camera underneath the belt. Only 10-20 seconds of footage was recorded to obtain ~40 indices of gait from the analysis software. The following parameters were measured: stance time, time elapsed while foot is in contact with the treadmill, in its stance phase; swing time, time elapsed while foot is in the air, in its swing phase; stride time, time elapsed between two successive

initiations of stances; brake time, time elapsed from the first contact with the treadmill to peak of stance; deceleration; propel time, time elapsed from peak stance to full swing.

Eyeblink conditioning in head-fixed mice

The apparatus and experimental procedure for eyeblink conditioning were previously described (Heiney et al., 2014). Briefly, mice were anesthetized with isoflurane (1.5–2% by volume) and positioned on the stereotaxic apparatus prepared for surgery. The skull was exposed, and two small holes were drilled on either side of the midline near bregma for inserting screws. A thin aluminum head plate was then placed over the bregma and the screws were fitted into the central hole in the head plate, which was affixed to the skull by Metabond cement.

Mice were habituated to head restraint for an hour in 3 habituation sesseions on top of a foam cylinder with the head fixed before start of the conditioning sessions. Mice were exposed to either a 240 ms blue LED light positioned 20 cm in front of the mouse or a 240 ms tone of white noise delivered via a speaker (4-Ω magnetic speaker, FF1, TDT) as a conditioned stimulus (CS). The volume of the white noise was set to just below the threshold that causes transient startle movement of the eyelid. The unconditioned stimulus (US) was a periocular air puff (30 – 40 psi) of 40 ms duration and delivered via a 23 gauge needle placed 5 mm from the mouse's cornea. The pressure of the periocular air puff was set for each mouse to induce a full reflexive blink as the unconditional response (UR). The CS-US inter-stimulus interval was 200 ms. Mice received 100 trials (80 CS-US paired trials and 20 CS-only trials) per day for 14 days. Eyelid movement was detected under infrared illumination using a high-speed (200 or 350 frames/s) monochrome video camera (Allied Vision). Eyelid positions, ranging from 1 (fully closed) to 0 (fully opened), were determined as the fraction of eyelid closure (FEC) using custom MATLAB software and the Video

Acquisition Toolbox. The FEC represents the proportion of the distance between the two eyelids. The response was considered to be a conditioned response (CR) if the FEC exceeded 0.2 after the CS onset but before the US.

Electrophysiology recording

Cerebella from P21 to P30 were retrieved and embedded in agarose while affixed to the specimen holder using adhesive glue. 300 mm thick sagittal slices of cerebellar vermis were prepared using a vibrating microtome (VT1000S, Leica) in oxygenated prechilled medium containing 125 mM NaCl, 2.5 mM KCl, 4 mM MgCl2, 1.25 mM KH2PO4, 26 mM NaHCO3, 1 m CaCl2, and 25 mM D-glucose (pH 7.3–7.4). The slices were then transferred to a recording chamber and superfused with artificial cerebrospinal fluid (aCSF) and gassed with a mixture of 95% O_2/5% CO_2 >1 hour at ice-cold temperature before recordings. Whole-cell recordings from Purkinje cells in cerebellar lobules 4-7 (voltage-clamped at –60 mV) were performed at room temperature with borosilicate glass pipettes (2–4 MΩ) pulled with a vertical micropipette puller (PC-10, Narishige). Recording electrodes were filled with internal solution containing 140 mM CsCl, 4 mM NaCl, 0.5 mM CaCl2, 10 mM HEPES, 5 mM EGTA, 2 mM Mg-ATP and 0.4 mM GTP (pH 7.3). For sIPSCs recording, 10 mM 6-Cyano-7-nitroquinoxaline-2,3-dione (CNQX) and 50 to 100 mM amino-5 phosphonopentanoic acid (APV) were added to the external solution to block glutamate receptor-mediated sEPSCs. Membrane currents were recorded using a Multiclamp 700B amplifier (Axon Instruments) connected to a DigiData 1440 (Molecular Devices) using pClamp 10.2 software (Molecular Devices). Series resistance (8–14 MΩ) was monitored throughout the experiments, and experimental data were discarded if the value changed by >20%. All signals were filtered at 2 kHz and sampled at 5–10 kHz. sIPSCs were analyzed with a threshold of 10 pA. Postsynaptic currents

were analyzed using Clampfit 11 software (Molecular Devices). Amplitudes and inter-event-interval were measured as a mean of the values obtained from 5 min recording sessions and analyzed using Prism software 8 (GraphPad) for statistical analysis and graphic presentations.

ERG and VEP Recordings

Mice were dark-adapted overnight, dilated with 1% tropicamide for 10 min, and anesthetized with 20/8/0.8 mg/kg ketamine/xylazine/urethane. Anesthetized mice were placed on the warmed surface of the Celeris ERG system (Diagnosys LLC, Lowell, MA) and corneal electrodes were placed on eyes lubricated with Genteel eye drops. Subdermal platinum needle electrodes were placed in the snout and tail as reference and ground electrodes, respectively. Additional platinum electrodes were placed on the right and left sides of the back of the head, near the visual cortex. The ERG and VEP were recorded sequentially during the same session. For the ERG recording, mice were exposed to 15 flashes of 1Hz, 1cd.s/m^2 white light. For the VEP recording, mice were exposed to 50 flashes of 1Hz, 0.5 cd.s/m^2 white light. At the end of the session, mice recovered on a warm pad and then were returned to their cage.

Quantifications and Statistical Analysis

NIH Image J software was used to measure the area (μm^2) for regions of interest (ROI) and for the acquisition of cell counting. For each stage, four to six midsagittal sections (approximately 10 um thick) of each cerebellum were used for quantitative analysis. For quantification of cells in the white matter, inner granule layer and molecular layer, the entire laminate was used as ROIs. Cells were counted using Image J plugin Cell counter or Nucleus counter according to the subcellular distribution of target antigen. For quantification of synapses, four to five 5000 μm^2 rectangular

ROIs in the molecular layer of lobule IV and V per sample were used. Positively stained puncta were counted by Image J plugin PunctaAnalyzer. All quantitative data were analyzed using Prism software 8 (GraphPad) for statistical analysis and graphic presentations. Unpaired student's t-test was used to compare the statistical difference between control and conditional mutant animals.

REFERENCES

Altman, J., and Bayer, S.A. (1997). Development of the Cerebellar System in relation to its evolution, structure, and function.

Asada, H., Kawamura, Y., Maruyama, K., Kume, H., Ding, R., Ji, F.Y., Kanbara, N., Kuzume, H., Sanbo, M., Yagi, T., et al. (1996). Mice Lacking the 65 kDa Isoform of Glutamic Acid Decarboxylase (GAD65) Maintain Normal Levels of GAD67 and GABA in Their Brains but Are Susceptible to Seizures. Biochem Bioph Res Co *229*, 891–895.

Bai, C.B., Auerbach, W., Lee, J.S., Stephen, D., and Joyner, A.L. (2002). Gli2, but not Gli1, is required for initial Shh signaling and ectopic activation of the Shh pathway. Development (Cambridge, England) *129*, 4753–4761.

Bai, C.B., Stephen, D., and Joyner, A.L. (2004). All mouse ventral spinal cord patterning by hedgehog is Gli dependent and involves an activator function of Gli3. Developmental Cell *6*, 103–115.

Beckinghausen, J., and Sillitoe, R.V. (2018). Insights into cerebellar development and connectivity. Neurosci Lett *688*, 2–13.

Blot, A., and Barbour, B. (2014). Ultra-rapid axon-axon ephaptic inhibition of cerebellar Purkinje cells by the pinceau. Nat Neurosci *17*, 289–295.

Brinke, M.M. ten, Boele, H.-J., Spanke, J.K., Potters, J.-W., Kornysheva, K., Wulff, P., IJpelaar, A.C.H.G., Koekkoek, S.K.E., and Zeeuw, C.I.D. (2015). Evolving Models of Pavlovian Conditioning: Cerebellar Cortical Dynamics in Awake Behaving Mice. Cell Reports *13*, 1977–1988.

Brown, A.M., Arancillo, M., Lin, T., Catt, D.R., Zhou, J., Lackey, E.P., Stay, T.L., Zuo, Z., White, J.J., and Sillitoe, R.V. (2019). Molecular layer interneurons shape the spike activity of cerebellar Purkinje cells. Nature Publishing Group 1–19.

Buch, T., Heppner, F.L., Tertilt, C., Heinen, T.J.A.J., Kremer, M., Wunderlich, F.T., Jung, S., and Waisman, A. (2005). A Cre-inducible diphtheria toxin receptor mediates cell lineage ablation after toxin administration. Nat Methods *2*, 419–426.

Cadilhac, C., Bachy, I., Forget, A., Hodson, D.J., Jahannault-Talignani, C., Furley, A.J., Ayrault, O., Mollard, P., Sotelo, C., and Ango, F. (2021). Excitatory granule neuron precursors orchestrate laminar localization and differentiation of cerebellar inhibitory interneuron subtypes. Cell Reports *34*, 108904.

Cameron, D.B., Kasai, K., Jiang, Y., Hu, T., Saeki, Y., and Komuro, H. (2009). Four distinct phases of basket/stellate cell migration after entering their final destination (the molecular layer) in the developing cerebellum. Dev Biol *332*, 309–324.

Costantini, F. (2016). Kidney Development, Disease, Repair and Regeneration. Sect Dev 41–56.

Dahmane, N., and Altaba, A.R. i (1999). Sonic hedgehog regulates the growth and patterning of the cerebellum. Development (Cambridge, England) *126*, 3089-100.

Feng, J., Meyer, C.A., Wang, Q., Liu, J.S., Liu, X.S., and Zhang, Y. (2012). GFOLD: a generalized fold change for ranking differentially expressed genes from RNA-seq data. Bioinformatics *28*, 2782–2788.

Fleming, J.T., He, W., Hao, C., Ketova, T., Pan, F.C., Wright, C.C.V., Litingtung, Y., and Chiang, C. (2013). The Purkinje neuron acts as a central regulator of spatially and functionally distinct cerebellar precursors. Developmental Cell *27*, 278–292.

Fujitani, Y., Fujitani, S., Luo, H., Qiu, F., Burlison, J., Long, Q., Kawaguchi, Y., Edlund, H., MacDonald, R.J., Furukawa, T., et al. (2006). Ptf1a determines horizontal and amacrine cell fates during mouse retinal development. Development *133*, 4439–4450.

Glasgow, S.M., Henke, R.M., Macdonald, R.J., Wright, C.V., and Johnson, J.E. (2005). Ptf1a determines GABAergic over glutamatergic neuronal cell fate in the spinal cord dorsal horn. Development (Cambridge, England) *132*, 5461–5469.

Heiney, S.A., Wohl, M.P., Chettih, S.N., Ruffolo, L.I., and Medina, J.F. (2014). Cerebellar-Dependent Expression of Motor Learning during Eyeblink Conditioning in Head-Fixed Mice. Journal of Neuroscience *34*, 14845–14853.

Hoshino, M., Nakamura, S., Mori, K., Kawauchi, T., Terao, M., Nishimura, Y.V., Fukuda, A., Fuse, T., Matsuo, N., Sone, M., et al. (2005). Ptf1a, a bHLH transcriptional gene, defines GABAergic neuronal fates in cerebellum. Neuron *47*, 201–213.

Huang, X., Ketova, T., Fleming, J.T., Wang, H., Dey, S.K., Litingtung, Y., and Chiang, C. (2009). Sonic hedgehog signaling regulates a novel epithelial progenitor domain of the hindbrain choroid plexus. Development (Cambridge, England) *136*, 2535–2543.

Huard, J.M., Forster, C.C., Carter, M.L., Sicinski, P., and Ross, M.E. (1999). Cerebellar histogenesis is disturbed in mice lacking cyclin D2. Dev Camb Engl *126*, 1927–1935.

Jain, S., Golden, J.P., Wozniak, D., Pehek, E., Johnson, E.M., and Milbrandt, J. (2006). RET Is Dispensable for Maintenance of Midbrain Dopaminergic Neurons in Adult Mice. J Neurosci *26*, 11230–11238.

Jeong, J., Mao, J., Tenzen, T., Kottmann, A.H., and McMahon, A.P. (2004). Hedgehog signaling in the neural crest cells regulates the patterning and growth of facial primordia. Genes & Development *18*, 937–951.

Kash, S.F., Johnson, R.S., Tecott, L.H., Noebels, J.L., Mayfield, R.D., Hanahan, D., and Baekkeskov, S. (1997). Epilepsy in mice deficient in the 65-kDa isoform of glutamic acid decarboxylase. Proc National Acad Sci *94*, 14060–14065.

Kawaguchi, Y., Cooper, B., Gannon, M., Ray, M., MacDonald, R.J., and Wright, C.V.E. (2002). The role of the transcriptional regulator Ptf1a in converting intestinal to pancreatic progenitors. Nat Genet *32*, 128–134.

Kopinke, D., Brailsford, M., Pan, F.C., Magnuson, M.A., Wright, C.V.E., and Murtaugh, L.C. (2012). Ongoing Notch signaling maintains phenotypic fidelity in the adult exocrine pancreas. Dev Biol *362*, 57–64.

Korn, H., and Axelrad, H. (1980). Electrical inhibition of Purkinje cells in the cerebellum of the rat. Proc National Acad Sci *77*, 6244–6247.

Lake, J.I., and Heuckeroth, R.O. (2013). Enteric nervous system development: migration, differentiation, and disease. Am J Physiol-Gastr L *305*, G1–G24.

Leto, K., Carletti, B., Williams, I.M., Magrassi, L., and Rossi, F. (2006). Different Types of Cerebellar GABAergic Interneurons Originate from a Common Pool of Multipotent Progenitor Cells. J Neurosci *26*, 11682–11694.

Leto, K., Bartolini, A., Yanagawa, Y., Obata, K., Magrassi, L., Schilling, K., and Rossi, F. (2009). Laminar Fate and Phenotype Specification of Cerebellar GABAergic Interneurons. Journal of Neuroscience *29*, 7079–7091.

Long, F., Zhang, X.M., Karp, S., Yang, Y., and McMahon, A.P. (2001). Genetic manipulation of hedgehog signaling in the endochondral skeleton reveals a direct role in the regulation of chondrocyte proliferation. Dev Camb Engl *128*, 5099–5108.

Machold, R., and Fishell, G. (2005). Math1 is expressed in temporally discrete pools of cerebellar rhombic-lip neural progenitors. Neuron *48*, 17–24.

Madisen, L., Zwingman, T.A., Sunkin, S.M., Oh, S.W., Zariwala, H.A., Gu, H., Ng, L.L., Palmiter, R.D., Hawrylycz, M.J., Jones, A.R., et al. (2010). A robust and high-throughput Cre reporting and characterization system for the whole mouse brain. Nat Neurosci *13*, 133–140.

Mao, J., Ligon, K.L., Rakhlin, E.Y., Thayer, S.P., Bronson, R.T., Rowitch, D., and McMahon, A.P. (2006). A novel somatic mouse model to survey tumorigenic potential applied to the Hedgehog pathway. Cancer Res *66*, 10171–10178.

Medina, J.F., Nores, W.L., Ohyama, T., and Mauk, M.D. (2000). Mechanisms of cerebellar learning suggested by eyelid conditioning. Curr Opin Neurobiol *10*, 717–724.

Mendelsohn, C., Batourina, E., Fung, S., Gilbert, T., and Dodd, J. (1999). Stromal cells mediate retinoid-dependent functions essential for renal development. Dev Camb Engl *126*, 1139–1148.

Orchard, P., White, J.S., Thomas, P.E., Mychalowych, A., Kiseleva, A., Hensley, J., Allen, B., Parker, S.C.J., and Keegan, C.E. (2018). Genome-wide chromatin accessibility and transcriptome profiling show minimal epigenome changes and coordinated transcriptional dysregulation of hedgehog signaling in Danforth's short tail mice. Hum Mol Genet *28*, 736–750.

Palay, S.L., and Chan-Palay, V. (1974a). Cerebellar Cortex, Cytology and Organization. 242–287.

Palay, S.L., and Chan-Palay, V. (1974b). Cerebellar Cortex-Cytology and Organization.

Parmigiani, E., Leto, K., Rolando, C., Figueres-Oñate, M., López-Mascaraque, L., Buffo, A., and Rossi, F. (2015). Heterogeneity and Bipotency of Astroglial-Like Cerebellar Progenitors along the Interneuron and Glial Lineages. J Neurosci *35*, 7388–7402.

Pascual, M., Abasolo, I., Meur, A.M.-L., Martinez, A., Rio, J.A.D., Wright, C.V., Real, F.X., and Soriano, E. (2007). Cerebellar GABAergic progenitors adopt an external granule cell-like phenotype in the absence of Ptf1a transcription factor expression. Proceedings of the National Academy of Sciences of the United States of America *104*, 5193–5198.

Pieper, A., Rudolph, S., Wieser, G.L., Götze, T., Mießner, H., Yonemasu, T., Yan, K., Tzvetanova, I., Castillo, B.D., Bode, U., et al. (2019). NeuroD2 controls inhibitory circuit formation in the molecular layer of the cerebellum. Sci Rep-Uk *9*, 1448.

Raymond, J.L., and Medina, J.F. (2018). Computational Principles of Supervised Learning in the Cerebellum. Annu Rev Neurosci *41*, 233–253.

Sears, L.L., Finn, P.R., and Steinmetz, J.E. (1994). Abnormal classical eye-blink conditioning in autism. J Autism Dev Disord *24*, 737–751.

Sergaki, M.C., López-Ramos, J.C., Stagkourakis, S., Gruart, A., Broberger, C., Delgado-García, J.M., and Ibáñez, C.F. (2017). Compromised Survival of Cerebellar Molecular Layer

Interneurons Lacking GDNF Receptors GFRα1 or RET Impairs Normal Cerebellar Motor Learning. Cell Reports *19*, 1977–1986.

Silbereis, J., Cheng, E., Ganat, Y.M., Ment, L.R., and Vaccarino, F.M. (2009). Precursors with Glial Fibrillary Acidic Protein Promoter Activity Transiently Generate GABA Interneurons in the Postnatal Cerebellum. Stem Cells *27*, 1152–1163.

Simkin, J.E., Zhang, D., Rollo, B.N., and Newgreen, D.F. (2013). Retinoic Acid Upregulates Ret and Induces Chain Migration and Population Expansion in Vagal Neural Crest Cells to Colonise the Embryonic Gut. Plos One *8*, e64077.

Somogyu, P., and Hámori, J. (1976). A quantitative electron microscopic study of the purkinje cell axon initial segment. Neuroscience *1*, 361-IN3.

Sotelo, C. (2015). Molecular Layer Interneurons of the Cerebellum: Developmental and Morphological Aspects. The Cerebellum *14*, 534–556.

Sudarov, A., Turnbull, R.K., Kim, E.J., Lebel-Potter, M., Guillemot, F., and Joyner, A.L. (2011). Ascl1 genetics reveals insights into cerebellum local circuit assembly. J Neurosci *31*, 11055–11069.

Wallace, V.A. (1999). Purkinje-cell-derived Sonic hedgehog regulates granule neuron precursor cell proliferation in the developing mouse cerebellum. Curr Biol. *9*, 445-8.

Wamsley, B., and Fishell, G. (2017). Genetic and activity-dependent mechanisms underlying interneuron diversity. Nat Rev Neurosci *18*, 299–309.

Wang, V.Y., Rose, M.F., and Zoghbi, H.Y. (2005). Math1 expression redefines the rhombic lip derivatives and reveals novel lineages within the brainstem and cerebellum. Neuron *48*, 31–43.

Wechsler-Reya, R.J., and Scott, M.P. (1999). Control of neuronal precursor proliferation in the cerebellum by Sonic Hedgehog. Neuron *22*, 103-14.

Weisheit, G., Gliem, M., Endl, E., Pfeffer, P.L., Busslinger, M., and Schilling, K. (2006). Postnatal development of the murine cerebellar cortex: formation and early dispersal of basket, stellate and Golgi neurons. Eur J Neurosci *24*, 466–478.

Wulff, P., Schonewille, M., Renzi, M., Viltono, L., Sassoè-Pognetto, M., Badura, A., Gao, Z., Hoebeek, F.E., Dorp, S. van, Wisden, W., et al. (2009). Synaptic inhibition of Purkinje cells mediates consolidation of vestibulo-cerebellar motor learning. Nat Neurosci *12*, 1042–1049.

Yamanaka, H., Yanagawa, Y., and Obata, K. (2004). Development of stellate and basket cells and their apoptosis in mouse cerebellar cortex. Neurosci Res *50*, 13–22.

Zhang, L., and Goldman, J.E. (1996). Generation of cerebellar interneurons from dividing progenitors in white matter. Neuron *16*, 47–54.

Zhou, J., Brown, A.M., Lackey, E.P., Arancillo, M., Lin, T., and Sillitoe, R.V. (2020). Purkinje cell neurotransmission patterns cerebellar basket cells into zonal modules defined by distinct pinceau sizes. Elife *9*, e55569.

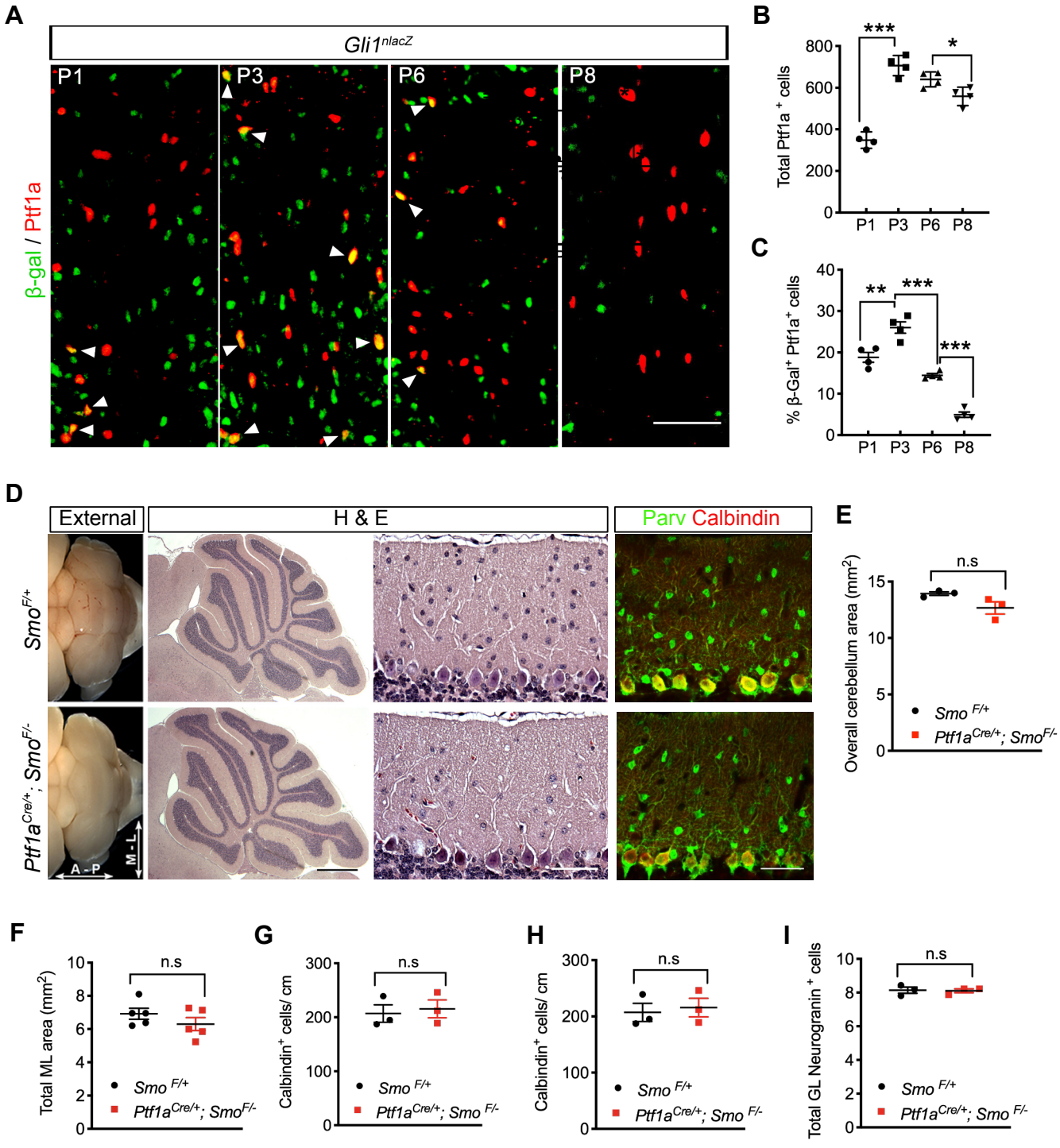

Figure 1, Li et al.

Figure 1. Shh signaling is transiently activated in Ptf1a+ progenitors and is required for MLI expansion.

(A) Midsagittal sections of *Gli1*^{nlacZ} mice showing β-gal and Ptf1a expression in PWM at P1, P3, P6 and P8. Arrowheads indicate cells co-express β-gal and Ptf1a. Scale bars indicate 50 μm.

(B and C) Quantification of total Ptf1a $^{+}$ cells (B) and the percentage of β-gal $^{+}$/Ptf1a^{+} double-positive cells (C) in the PWM. N= 4 mice per group.

(D) Brains from *Smo* $^{F/+}$ and *Ptf1a*$^{Cre/+;}$ *Smo*$^{F/-}$ animals at P21 showing external views and H&E stained sections.

(E and F) Quantification of the overall midsagittal area of the cerebellum and the molecular layer in P21 *Smo* $^{F/+}$and *Ptf1a*$^{Cre/+;}$ *Smo* $^{F/-}$ mice. N= 3 to 5 mice per group.

(G) Midsagittal cerebellar sections from P21 *Smo* $^{F/+}$and *Ptf1a*$^{Cre/+;}$ *Smo* $^{F/-}$ mice stained with antibodies against parvalbumin (Parv) and calbindin. Scale bars indicate 50 μm.

(H-J) Quantitative analysis of Parv^{+} interneurons (H), calbindin+ Purkinje cells (I) and Neurogranin+ Golgi cells (J) in P21 *Smo* $^{F/+}$and *Ptf1a*$^{Cre/+;}$ *Smo* $^{F/-}$ cerebella. N= 5 mice per group.

(K) The length of Purkinje cells' dendritic spines in P21 *Smo* $^{F/+}$and *Ptf1a*$^{Cre/+;}$ *Smo* $^{F/-}$ cerebella. N= 3 mice per group.

All graphs displayed are mean ± SEM. *p ≤ 0.05, **p ≤ 0.01, ***p ≤ 0.001. n.s., not significant.

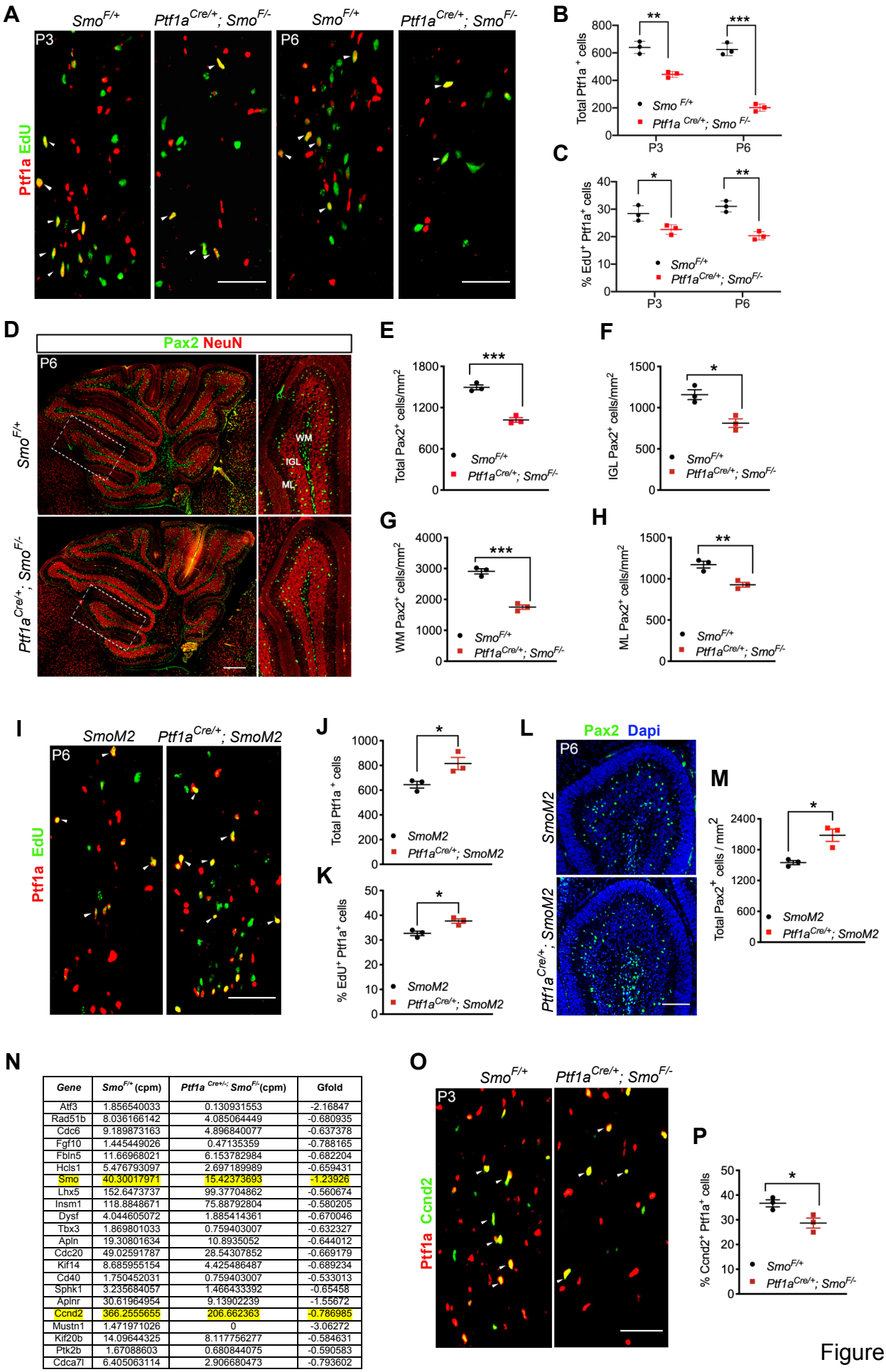

Gene	Smo F/+ (cpm)	Ptf1a Cre+/-; Smo F/- (cpm)	Gfold
Atf3	1.856540033	0.130931553	-2.16847
Rad51b	8.036166142	4.085064449	-0.680935
Cdc6	9.189873163	4.896840077	-0.637378
Fgf10	1.445449026	0.47135359	-0.788165
Fbln5	11.66968021	6.153782984	-0.682204
Hcls1	5.476793097	2.697189989	-0.659431
Smo	40.30017971	15.42373693	-1.23926
Lhx5	152.6473737	99.37704862	-0.560674
Insm1	118.8848671	75.88792804	-0.580205
Dysf	4.044605072	1.885414361	-0.670046
Tbx3	1.869801033	0.759403007	-0.632327
Apln	19.30801634	10.8935052	-0.644012
Cdc20	49.02591787	28.54307852	-0.669179
Kif14	8.685955154	4.425486487	-0.689234
Cd40	1.750452031	0.759403007	-0.533013
Sphk1	3.235684057	1.466433392	-0.65458
Aplnr	30.61964954	9.13902239	-1.55672
Ccnd2	366.2555655	206.662363	-0.786985
Mustn1	1.471971026	0	-3.06272
Kif20b	14.09644325	8.117756277	-0.584631
Ptk2b	1.67088603	0.680844075	-0.590583
Cdca7l	6.405063114	2.906680473	-0.793602

Figure 2, Li et al.

Figure 2. Shh signaling promotes Ptf1a+ progenitor proliferation and the expansion of Pax2^{+} immature interneurons.

(A-F) Ptf1a and EdU staining in PWM of *Smo* $^{F/+}$and *Ptf1a*$^{Cre/+;}$ *Smo* $^{F/-}$ cerebella at P3 (A-C) and P6 (D-F). Arrowheads indicate cells positive for both EdU and Ptf1a. Quantification of total Ptf1a $^{+}$ cells in the PWM at P3(B) and P6 (E). The percentage of EdU $^{+}$/Ptf1a^{+} double-positive cells relative to the total number of Ptf1a^{+} cells in PWM at P3 (C) and P6 (F) is also quantified. N= 3 mice per group. Scale bars indicate 50 μm.

(G) Pax2 and NeuN staining in sagittal sections of *Smo* $^{F/+}$and *Ptf1a*$^{Cre/+;}$ *Smo* $^{F/-}$ cerebella. A higher magnification view of boxed regions is shown on the right. Abbreviations: WM, white matter; IGL, inner granule layer; ML, molecular layer. Scale bars indicate 100 μm.

(H-K) Quantitative analysis of Pax2+ cells in different regions of the cerebellum shown in G. N= 3 mice per group.

(L) Ptf1a and EdU staining in PWM of *SmoM2 and Ptf1a*$^{Cre/+}$*; SmoM2* mice at P6. Arrowheads indicate cells positive for both EdU and Ptf1a. Scale bars indicate 50 μm.

(M-N) Quantitative analysis of total Ptf1a $^{+}$ cells (M) and the percentage of EdU $^{+}$/Ptf1a^{+} double-positive cells relative to the total number of Ptf1a^{+} cells (N) in PWM at P6.

(O) Pax2 staining in the ML of *SmoM2 and Ptf1a*$^{Cre/+}$*; SmoM2* mice at P6. Scale bars indicate 100 μm.

(P) Quantitative analysis of Pax2^{+} cells shown in O. n= 3 mice per group.

(Q) List of genes associated with positive regulation of cell proliferation identified by RNA-seq analysis. Ccnd2 is highlighted in yellow.

(R) Ptf1a and Ccnd2 staining in PWM of *SmoM2 and Ptf1a*$^{Cre/+}$*; Smo* $^{F/-}$ mice at P6. Arrowheads indicate cells co-expressing Ccnd2 and Ptf1a. Scale bars indicate 50 μm.

(S) Quantitative analysis of the percentage of Ccnd2 and Ptf1a double-positive cells relative to the total number of Ptf1a^{+} cells in PWM at P6. N= 3 mice per group.

All graphs displayed are mean ± SEM. *p ≤ 0.05, **p ≤ 0.01, ***p ≤ 0.001. n.s., not significant.

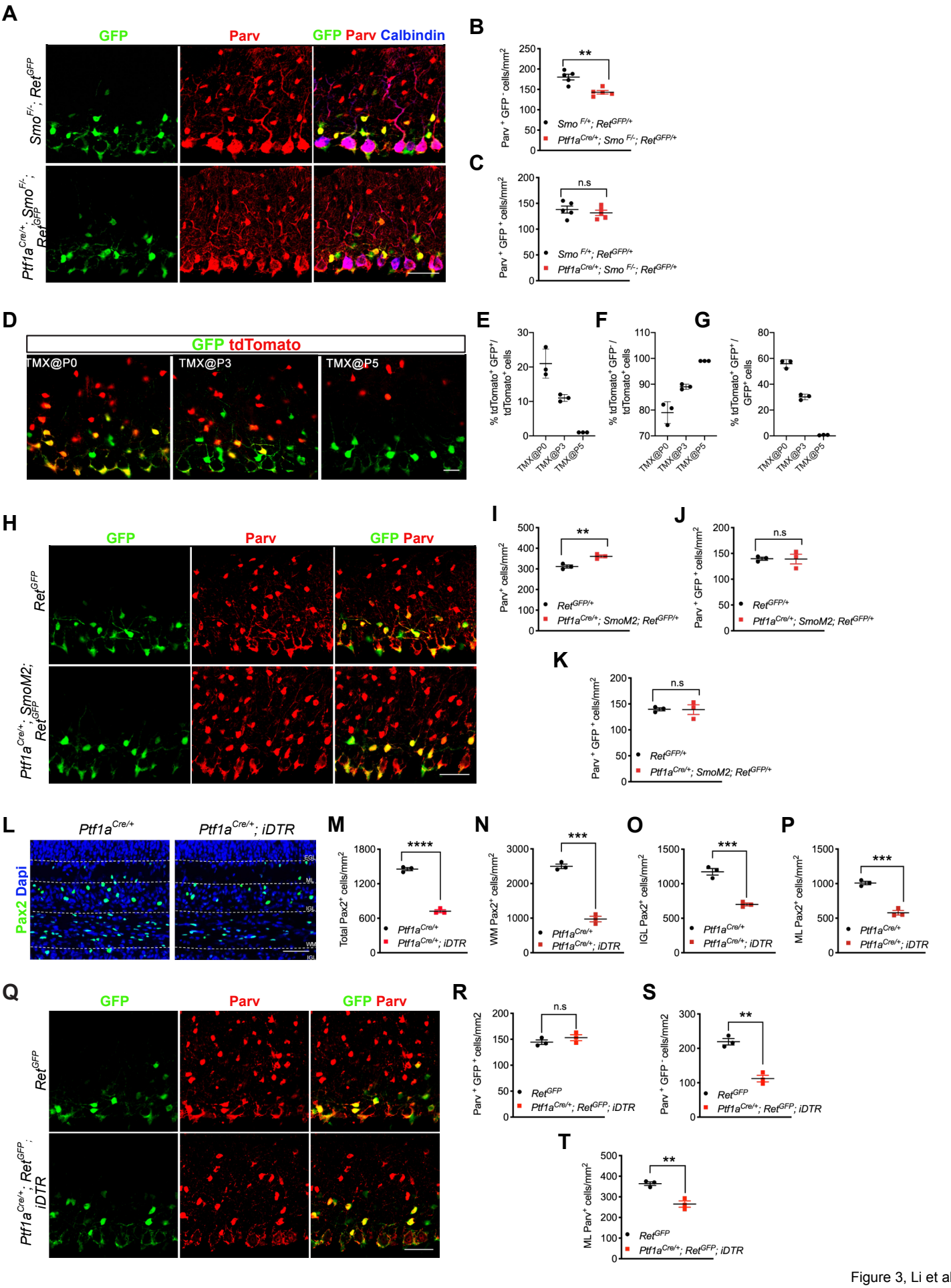

Figure 3, Li et al.

Figure 3. Shh signaling selectively regulates stellate cell pool size.

(A) Cerebellar sections from P21 *Smo* $^{F/+}$; *Ret*$^{GFP/+}$ *and Ptf1a*$^{Cre/+}$*; Smo*$^{F/-}$*; Ret*$^{GFP/+}$ mice stained with antibodies against GFP, Parvalbumin and Calbindin.

(B-C) Quantitative analysis of Parv^{+} GFP^{+} (B) and Parv^{+} GFP^{-} (C) cells shown in A. N= 5 mice per group.

(D) Cerebellar sections from P21 *Ptf1a*$^{Cre/+}$*; R26R*^{Ai9}*; Ret*$^{GFP/+}$ mice showing the extent of BC labeling (dtTomato^{+} GFP^{+}) following TMX induction at P0, P3 or P5.

(E-F) Quantitative analysis of the percentage of labeled BCs (dtTomato^{+} GFP^{+}) and SCs (dtTomato^{+} GFP^{-}) relative to total labeled (dtTomato^{+}) cells.

(G) Quantitative analysis of the percentage of labeled BCs (dtTomato^{+} GFP^{+}) relative to total GFP+ BCs.

(H) Cerebellar sections from P21 *Ret*$^{GFP/+}$ *and Ptf1a*$^{Cre/+}$*; SmoM2; Ret*$^{GFP/+}$ mice stained with antibodies against GFP and Parvalbumin.

(I-K) Quantitative analysis of Parv+ (I), Parv^{+} GFP^{+} (J) and Parv^{+} GFP^{-} (K) cells shown in H. N= 3 mice per group.

(L) Cerebellar sections from P6 *Ret*$^{GFP/+}$ and *Ptf1a*$^{Cre/+}$*; iDTR* mice showing Pax2 distribution (green) in EGL, IGL and WM following DT administration at P0-P2.

(M-P) Quantitative analysis of total Pax2+ cells (M) and Pax2+ cells in WM (N), IGL (O) and ML (P). N= 3 mice per group.

(Q) Cerebellar sections from P21 *Ret*$^{GFP/+}$ and *Ptf1a*$^{Cre/+}$*; iDTR* mice stained with antibodies against GFP and Parvalbumin.

(R-T) Quantitative analysis of Parv^{+} GFP^{+} (R), Parv^{+} GFP^{-} (S) and Parv^{+} (T) cells shown in A. N= 3 mice per group.

All graphs displayed are mean ± SEM. *p ≤ 0.05, **p ≤ 0.01, ***p ≤ 0.001. n.s., not significant.

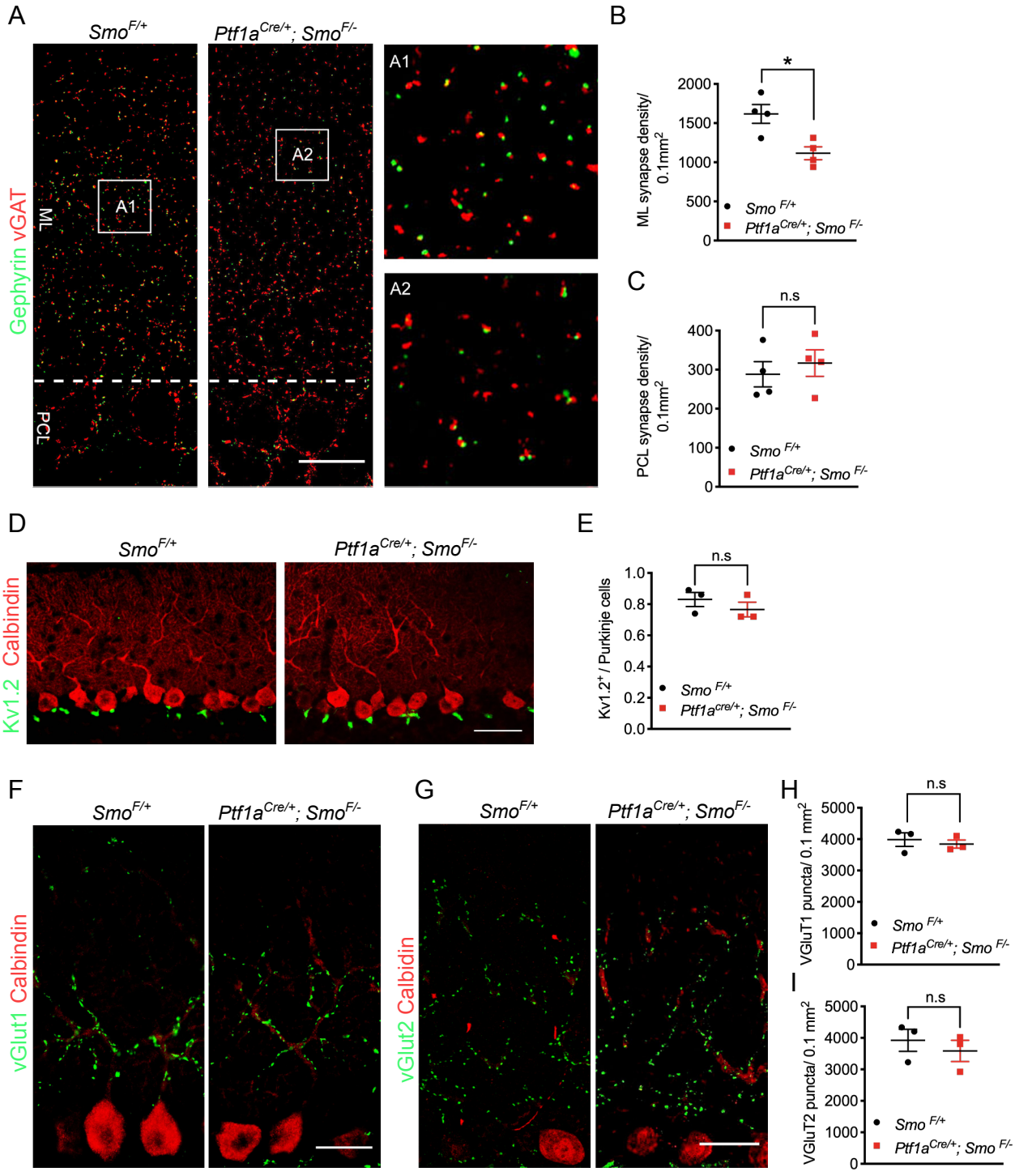

Figure 4, Li et al.

Figure 4. Loss of Shh-dependent stellate cells reduces ML GABAergic synapses.

(A-A2) Cerebellar sections from P21 *Smo* $^{F/+}$ *and Ptf1a*$^{Cre/+}$*; Smo*$^{F/-}$ mice stained with antibodies against vGAT and Gephyrin. A1 and A2 represent enlarged views of the boxed regions in A. ML, molecular layer. PCL, Purkinje cell layer. Scale bars indicate 25 μm.

(B-C) Quantitative analysis of vGAT and Gephyrin double-positive synapses in the ML (B) and PCL (C). N= 4 mice per group.

(D) Cerebellar sections from P21 *Smo* $^{F/+}$ *and Ptf1a*$^{Cre/+}$*; Smo*$^{F/-}$ mice stained with antibodies against Kv1.2 and calbindin. Scale bars indicate 50 μm.

(E) Quantitative analysis of Kv1.2 in PCL shown in D. N= 4 mice per group.

(F-G) Cerebellar sections from P21 *Smo* $^{F/+}$ *and Ptf1a*$^{Cre/+;}$ *Smo*$^{F/-}$ mice stained with antibodies against vGluT1 (F), vGluT2 (G) and calbindin. Scale bars indicate 25 μm.

(H and I) Quantitative analysis of vGluT1 and vGluT2 positive puncta in the ML. N= 3 mice per group.

All graphs displayed are mean ± SEM. *p ≤ 0.05, **p ≤ 0.01, ***p ≤ 0.001. n.s., not significant.

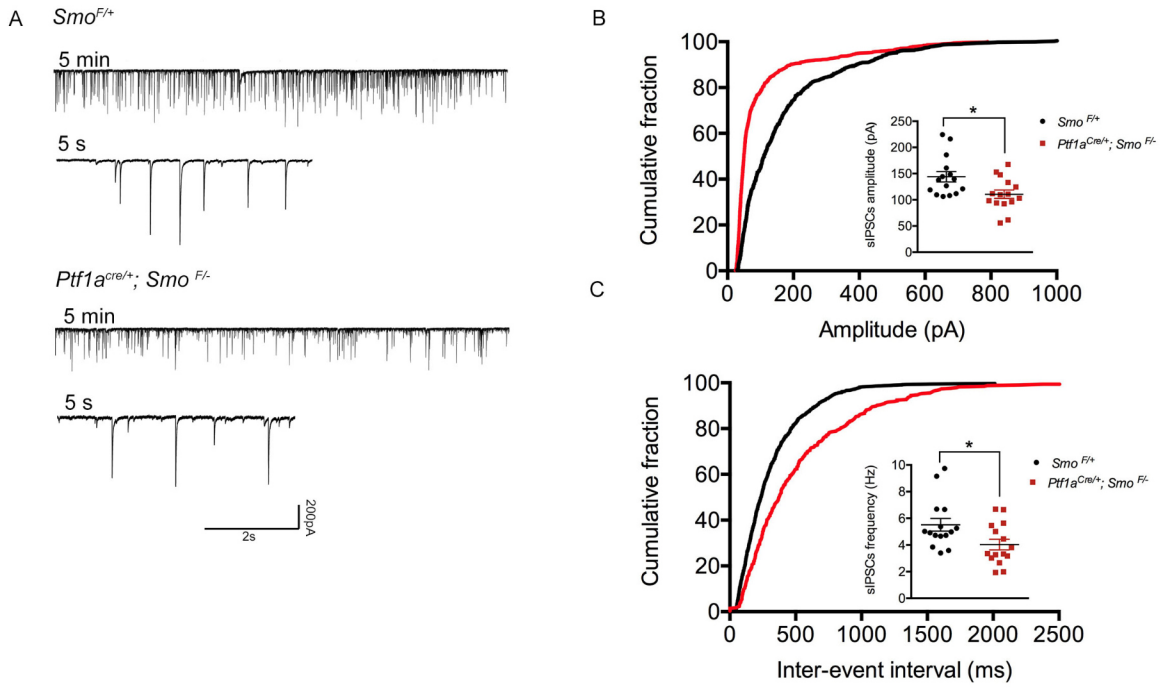

Figure 5, Li et al.

Figure 5. Decreased amplitude and interevent interval of sIPSCs in *Ptf1a$^{Cre/+}$; Smo$^{F/-}$* mutants.

(A) Representative traces of spontaneous IPSC recorded from *Smo $^{F/+}$ and Ptf1a$^{Cre/+}$; Smo $^{F/-}$* cerebellar Purkinje cells.

(B-C) Statistical analysis of sIPSCs amplitude (B) interevent interval (C). Each dot represents the mean of values obtained from 5 min recording sessions of individual PC. N= 15 cells from 11 *Smo $^{F/+}$* mice and 8 *Ptf1a$^{Cre/+}$; Smo $^{F/-}$* mice. Values represent mean ± SEM. * $p < 0.05$.

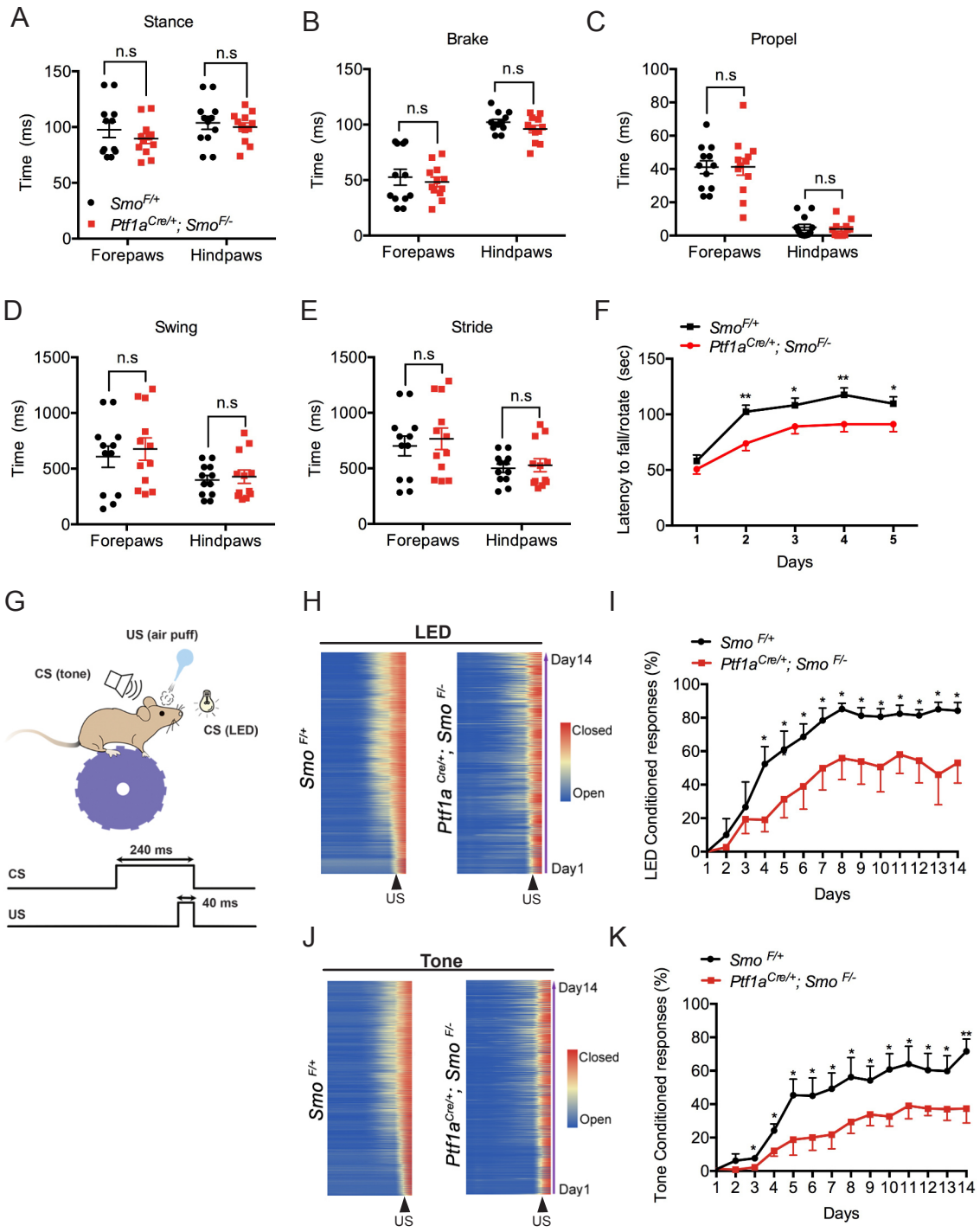

Figure 6, Li et al.

Figure 6. Shh-dependent SC pool is required for cerebellum-dependent motor learning but not basic motor function.

(A-E) Quantitative gait analysis of adult *Smo* $^{F/+}$ and *Ptf1a*$^{Cre/+}$*; Smo*$^{F/-}$ mice showing stance time (A), brake time (B), propel time (C), swing time (D) and stride time (E). N= 12 mice per group.

(F) Accelerating rotarod test to measure latency to fall on five consecutive days in *Smo* $^{F/+}$ and *Ptf1a*$^{Cre/+}$*; Smo*$^{F/-}$ mice. N= 30 mice per group.

(G) Schematic of eyeblink conditioning system. The trial structure is consists of a 240 ms blue light (CS) or tone (CS) that precedes and co-terminates with a 40 ms air puff (US).

(H-J) Group averages of trial-by-trial eyelid closure over the entire 14 days of conditioning with LED (H) or tone (J) in *Smo* $^{F/+}$ and *Ptf1a*$^{Cre/+}$*; Smo*$^{F/-}$ mice.

(I-K) The percentage of conditioned responses LED (I) or tone (K). N= 5 mice per group. All graphs displayed are mean ± SEM. * $p < 0.05$, **$p < 0.01$. n.s., not significant.